



This is a repository copy of *In-situ full-wafer metrology via coupled white light and monochromatic stroboscopic illumination*.

White Rose Research Online URL for this paper:

<https://eprints.whiterose.ac.uk/224533/>

Version: Published Version

Article:

Atkinson, J.B.P. orcid.org/0009-0002-6371-1953 and Howse, J.R. orcid.org/0000-0003-1503-2083 (2025) *In-situ full-wafer metrology via coupled white light and monochromatic stroboscopic illumination*. *Optics and Lasers in Engineering*, 184 (Part 2). 108692. ISSN 0143-8166

<https://doi.org/10.1016/j.optlaseng.2024.108692>

Reuse

This article is distributed under the terms of the Creative Commons Attribution (CC BY) licence. This licence allows you to distribute, remix, tweak, and build upon the work, even commercially, as long as you credit the authors for the original work. More information and the full terms of the licence here:

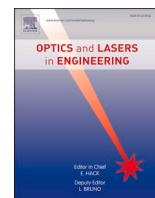
<https://creativecommons.org/licenses/>

Takedown

If you consider content in White Rose Research Online to be in breach of UK law, please notify us by emailing eprints@whiterose.ac.uk including the URL of the record and the reason for the withdrawal request.



eprints@whiterose.ac.uk
<https://eprints.whiterose.ac.uk/>



In-situ full-wafer metrology via coupled white light and monochromatic stroboscopic illumination

Jack B.P. Atkinson, Jonathan R. Howse*

Sir Robert Hadfield Building, School of Chemical, Materials and Biological Engineering, University of Sheffield, Mappin Street, Sheffield, South Yorkshire S13 JD, United Kingdom

ARTICLE INFO

Keywords:
Spin-coating
Metrology
Thin film interference
Reflectance
Full-wafer

ABSTRACT

This work presents a novel optical setup to provide scalable *in-situ* metrology during spin coating. Stroboscopic white light imaging provides high resolution color videos of the process, at a temporal resolution matching the spin speed, where thin film interference colors are observed. Monochromatic specular reflection intensity data from the center of rotation provides a thickness profile at this point. By developing a color to thickness relationship *in-situ* with the combination of these techniques and leveraging the large-area data provided by color imaging, the thickness at any point on the wafer is reconstructed via a mapping procedure with minimal a-priori information. Experiments are carried out on full 3" diameter wafers spun with pure xylene or pure butyl acetate, and the thickness profile at all points on the wafer can be determined. Differences in the topology of these solvents whilst drying are linked back to the solvent properties. The color to thickness mapping procedure is shown to have less than 5 % error in determined thickness values between 2 μ m and 100nm. The possible length scale resolved by the imaging is fully discussed as a function of radius, spin speed, strobe pulse duration and hardware used. The studies in this work achieved a minimum lateral resolution of 315 μ m when observing a full wafer, which is sufficiently detailed to properly reconstruct thickness variations caused by common spin-coating defects such as comets. The large area and scalable nature of this metrology technique lends itself to applications in semiconductor manufacturing where substrates of 300 mm are standard.

1. Introduction

Spin coating is an indispensable thin film fabrication technique, offering a simple and reliable approach for depositing thin films with robust control over thickness and morphology. These films find extensive applications across various fields, including photoresists and electronics [1,2], optoelectronics [3–5] and energy storage [6], among others. The exceptional versatility of spin coating lies in the techniques ability to accommodate a wide set of materials beyond the standard photoresist, ranging from polymer blends [7–9] to small molecule crystals [10] and colloids [11–14], enabling tailored film designs to suit specific application requirements. The effectiveness of each film in its application, regardless of specific morphology, is underpinned by a precise control of the thickness and uniformity.

Spin coating is one of the principal methods for fabricating thin films, especially at the lab scale. This is despite growing interest in larger scale or roll-to-roll (R2R) methods, such as slot-die coating, that are yet to close the gap in controllability and ease of use. Similarly, the dispensed

liquid volumes employed in spin-coating, compared to R2R, permits film fabrication with greater efficiencies of materials and costs at lab scale. As a highly non-equilibrium process, on time scales of seconds, it is challenging for researchers to gain insight into the interplaying dynamics occurring during spin coating. Conversely, it is exactly this that places it as such a fast and reproducible method for synthesizing these films. *In-situ* non-contact reflection and scattering techniques have repeatedly proved a powerful tool over the last three decades, allowing researchers deeper insight into the phenomena at play. This has led to the development of films with more complex and uniform morphology, unlocking optimal structures and affording increased functionality and higher performance.

Techniques such as spectroscopic ellipsometry (SE) [15], specular laser reflection [16,17], off-specular scattering [18], spectroscopy [19], wide-angle X-ray scattering (WAXS) [20] and grazing incidence x-ray diffraction (GIXRD) [21] have all been utilized *in-situ* to monitor spun coat films' thickness and/or morphology. While providing valuable information, these techniques are all limited to small areas and

* Corresponding author.

E-mail addresses: jatkinson6@sheffield.ac.uk (J.B.P. Atkinson), j.r.howse@sheffield.ac.uk (J.R. Howse).

<https://doi.org/10.1016/j.optlaseng.2024.108692>

Received 22 March 2024; Received in revised form 24 September 2024; Accepted 7 November 2024

Available online 15 November 2024

0143-8166/Crown Copyright © 2024 Published by Elsevier Ltd. This is an open access article under the CC BY license (<http://creativecommons.org/licenses/by/4.0/>).

consequently only effectively impart information at a single point, usually at the center of rotation to mitigate the effects of rotation and high angular velocities. This is a major drawback when spun coat films have the potential to vary in both thickness and morphology over the substrate, as evident in non-uniform films. Toolan et al. and Ebbens et al. utilized *in situ* reflectance imaging with stroboscopic illumination to enable direct microscopy of polymer phase separation during spin coating [22–24], observing how polymers phase separated with a thickness difference. These studies marked an improvement in the active area of the measurement compared to a point, and thus were able to resolve additional morphological information compared to specular reflectance. Bergqvist et al. performed *in situ* reflectance imaging to capture complete thickness information over a 3 cm² substrate [25]. Laser or monochromatic LED illumination is used in these imaging studies in combination with digital imaging so that thicknesses can be unambiguously extracted from pixel intensity information via fringe counting. However, in all these studies there is tension between the sampled area size and the lateral (surface metrology) resolution that is probed; the further from the center of rotation, the increase in radial velocity gives time averaged, and hence surface averaged, data.

Most of these previous studies have employed monochromatic illumination as an aid to straightforward height reconstruction; methods that combine broadband white light and digital imaging encounter additional complexities. The use of white light means that interference fringes denoting a specific change in thickness, such as those visible when single wavelength light is used, do not appear. In contrast, white light produces interference colors that are the sum of different wavelengths at different levels of reflectance, producing a rainbow-like pattern; the same effect causes the multicolor appearance in bubbles of soap. Birnie et al. used broadband white illumination across a 2" diameter silicon wafer to produce radially averaged thickness profiles by tracking interference colors outwards from a center point, where the thickness was determined via specular reflection. They directly observed that thickness increased towards the edge of the substrate [26]. These observations challenged existing models that suggested laminar airflow over the wafer and Newtonian liquid flow should result in thinning independent of radius. The data was radially averaged due to image sensor sensitivity and data capture/exposure times generating radially blurred images.

For an isotropic non-absorbing thin film system the reflectance spectrum is given by Eq. (1) [27], where r_{10} and r_{21} are the Fresnel coefficients of the film-substrate and the ambient-film interfaces, given by $\frac{n_0 - n_1}{n_0 + n_1}$, and $\frac{n_1 - n_2}{n_1 + n_2}$ where n_0 , n_1 and n_2 are the substrate, film and ambient refractive indices respectively, and the phase change caused by the optical path difference between subsequently reflected rays is $\delta_1 = \frac{2\pi n_1 d \cos(\theta_1)}{\lambda}$.

$$R(\lambda, d) = \frac{r_{10}^2 + r_{21}^2 + 2r_{10}r_{21} \cos(2\delta_1)}{1 + r_{10}^2 r_{21}^2 + 2r_{10}r_{21} \cos(2\delta_1)} \quad (1)$$

The reflectance spectrum is therefore dependent on the refractive indices of the system, the angle of refraction in the film (the angle of propagation in the film, found from the angle of incidence from Snell's law), θ_1 , the wavelength of light, λ , and the thickness of the film, d . When imaging, this spectrum R is captured by a digital camera sensor in a process modeled by Eq. (2).

$$x_i = \Gamma_i \left(b_i \xi_i \int_{\lambda_{\min}}^{\lambda_{\max}} I(\lambda) R(\lambda, d) B_i(\lambda) d\lambda + \epsilon_i \right) \quad (2)$$

Here, x_i represents the scalar response of each color channel $i = R, G, B$. $I(\lambda)$ denotes the illumination spectrum, $R(\lambda, d)$ is the reflectance spectrum of the thin film system, $B_i(\lambda)$ is the camera's sensitivity for the i^{th} channel. ϵ_i accounts for the random noise in the i^{th} channel, distributed with a mean of zero. The function Γ_i represents any nonlinearity in the channel, including camera gamma, color temperature, and non-

linear sensor response. The channel's color balance is denoted as b_i and the scalar ξ_i models the exposure settings, gain and geometry of the setup.

Thickness may no longer be unambiguously defined by the intensities of color channels alone. This is a well-documented limitation of color imaging to determine film thicknesses, not just in spin coating but in other areas such as foam [28,29] and lubricant [30] studies. This issue arises due to the loss of spectral information in digital imaging when a camera converts an incident spectrum to a RGB color triplet via Bayer filtering and integration by the sensor as shown by Eq. (2). A representation of this reduction in data is shown in Fig. 1, that uses Eq. (1) and 2 to simulate a color camera response to a PMMA film ($n = 1.49$, $k = 0$) of varying thickness on a silicon substrate ($n = 3.88$, $k = 0.02$), in air. Past efforts to mitigate the ambiguity have involved manual reference via colormaps [31], employing existing film profile knowledge [29,30,32], and the use of hyperspectral cameras [33].

The work presented here seeks to address the small-area limitations of other thickness measurement methods. It is enabled by recent high-speed, high sensitivity CMOS sensors, and high-power LED illumination and offers a novel technique that leverages digital color imaging to produce two-dimensional thickness maps of a spun coat solvents over full-wafer areas. These maps can be reconstructed with minimal system knowledge via a color-to-thickness relationship constructed *in-situ*. To achieve this an optical setup has been constructed around a spin coater that simultaneously performs stroboscopic white light imaging and laser spectral reflectance. The ambiguity arising from using broadband white light has been resolved by developing a thickness mapping algorithm that selects the most appropriate solution to the developed color-to-thickness relationship.

2. Materials and methods

2.1. Apparatus

2.1.1. Stroboscopic white light imaging

A custom-made spin coater has been installed under an array of 8 × 18v, 4000 K light emitting diodes (LED) (CXA1510-0000-000F0UG440H, CREE) outputting 6720 lm total, fitted with a 4 mm thick etched glass diffuser. A CMOS camera is mounted at 20° with a full, unobstructed view of the full wafer surface and chuck. The diffuser is larger than the wafer and despite the distance, fills the surface of the imaged wafer. The camera used is a Pixelink PL-X9512 containing a 17.6 mm (diagonal) Sony IMX235 sensor and is fitted with a 50 mm, $\frac{f}{2.2}$ lens. The spin coater is made from a twin-shaft MAXON EC-i brushless motor, controlled via Labview. During rotation, a pulse is generated at the same point in every rotation by an optical switch and is used to trigger the start of the camera's exposure which also generates a strobe pulse of 30μs width for the LED driver circuit, which powers the LED array at 31v, based upon circuitry reported by Willert et al. The short length of this pulse 'freezes' the wafer for a clear picture, this is discussed further in Section 3.3. High brightness LEDs are well suited to this application due to their rise time in the order of nanoseconds and ability to be run reliably in short pulses well over their rated power [34], ensuring sufficient illumination in the limited time. Data is collected continuously via 10GigE and solid-state M.2 drive (Fig. 2).

This produces one image per full rotation, resulting in a video where the wafer appears motionless and interference colors can be tracked through time at any point across the surface. Fig. 3 shows frames of a video captured in this way. The supplementary information contains examples of both the raw (S1–S3) and processed (S4–S6) versions of the videos, for full wafer xylene, full wafer butyl acetate and square wafer xylene respectively, shown at 15fps for clarity. Native speed would be 41.7fps (full wafer) or 33.3fps (square wafer) equivalent to spin speeds of 2500 rpm and 2000 rpm respectively.

In this study, a camera with a linear sensor response is used and any

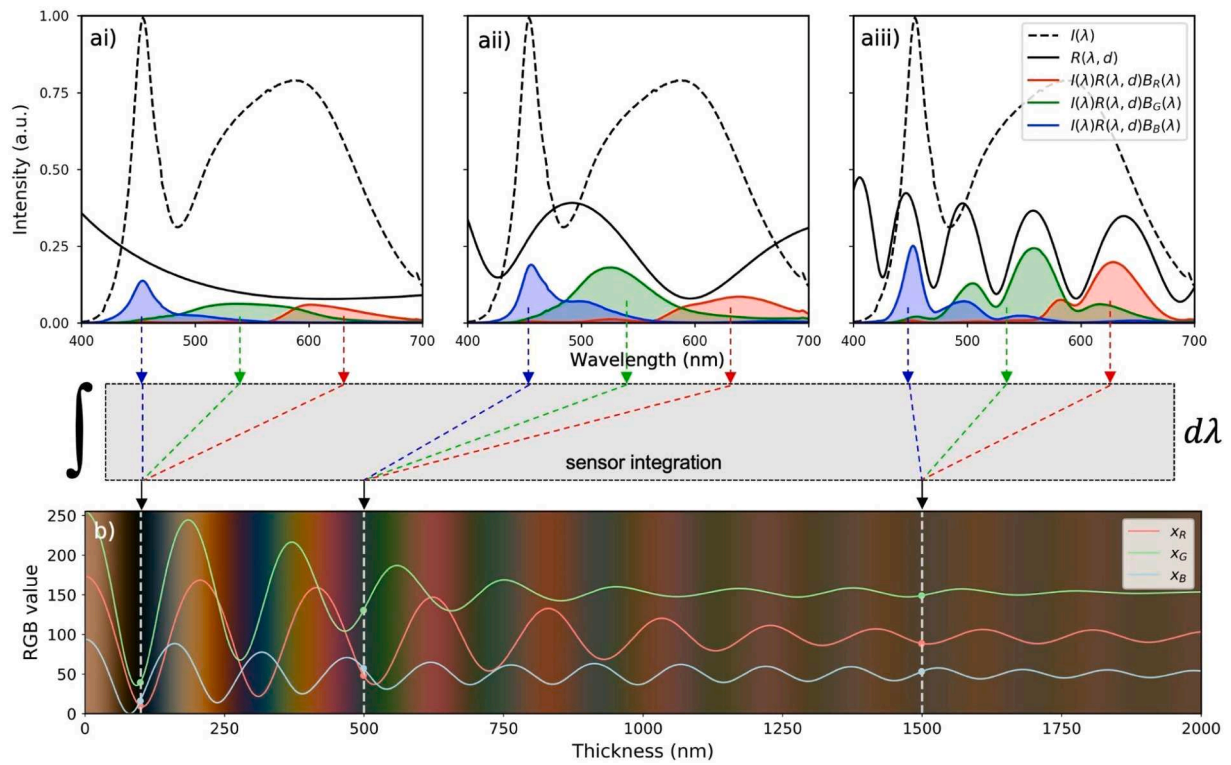


Fig. 1. Digital imaging of a thin film system; (a) simulated reflectance spectra and channel activation spectra when observing a PMMA film ($n = 1.49$) of 100 nm (i) 500 nm (ii) and 1500 nm (iii) thicknesses with a Sony IMX253 sensor and LED illumination. (b) The normalized RGB triplets for these channel activations as a function of thickness overlaid on the corresponding simulated colormap, where the green activation has been reduced by a factor of two to account for relative frequency in the Bayer filter mosaic.

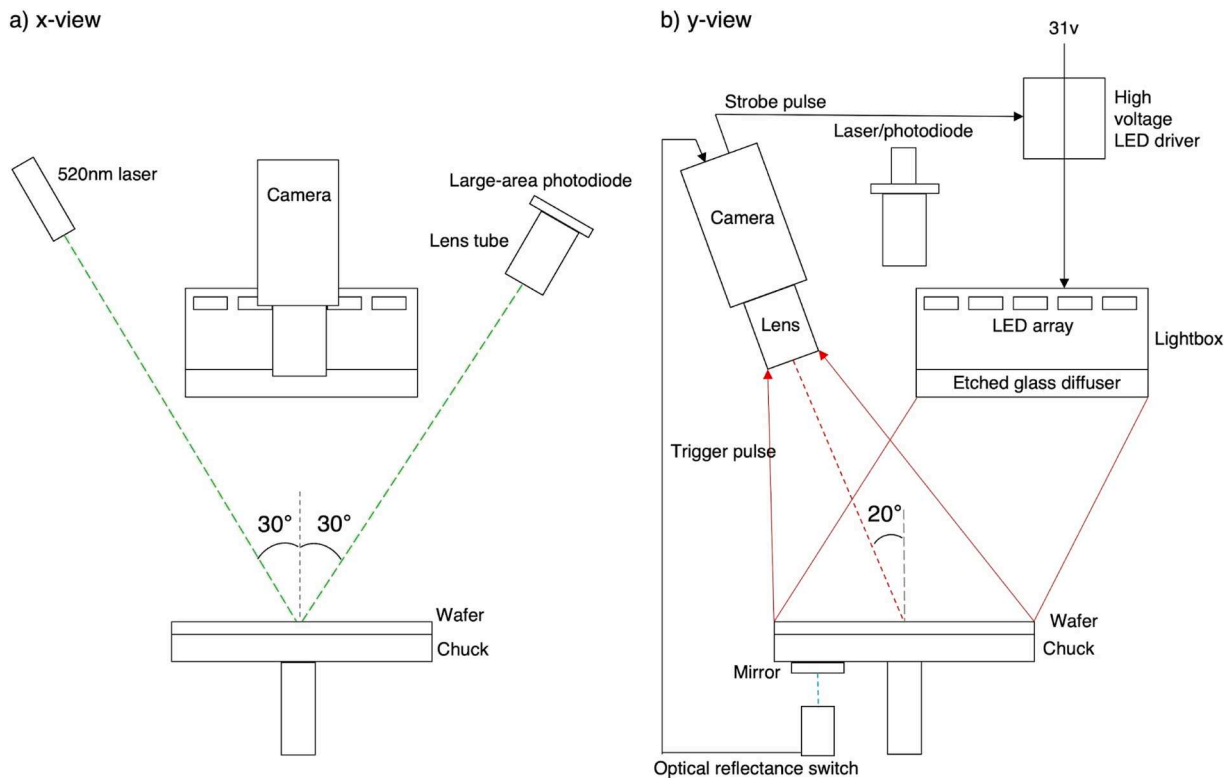


Fig. 2. A schematic diagram of the stroboscopic imaging and laser reflectance configuration around the spun coat wafer from two perpendicular points of view.

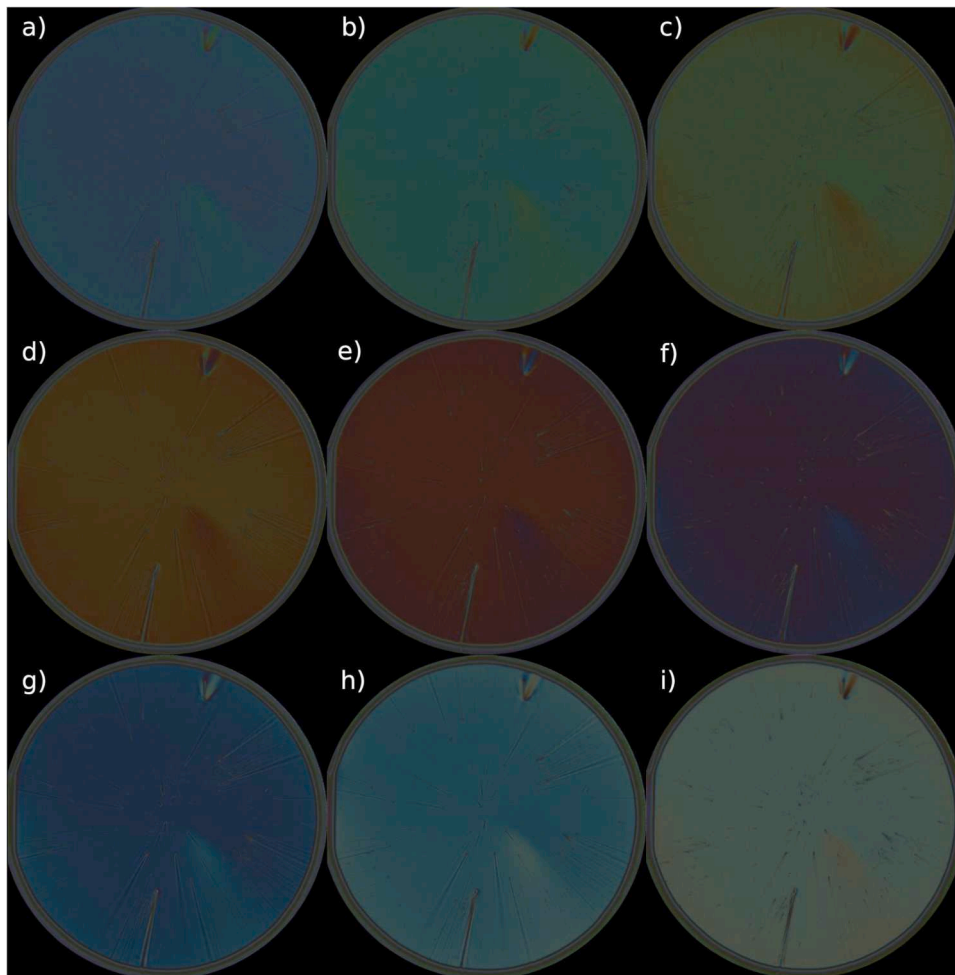


Fig. 3. A series of 9 stroboscopic images taken from a video of xylene spun on a 3" diameter wafer at 2500rpm. The images are spaced apart by 48ms. From (a) to (i) the centre thickness decreases from $0.399\mu\text{m}$ to $0.166\mu\text{m}$, with frame (i) being 277 ms before complete drying. Cyclical interference colors can be observed due to the thinning of the film. Edge beads, comet defects, and fluid nonuniformity can be clearly identified qualitatively by color change within each frame.

gamma or color temperature correction was disabled, removing the nonlinear function, Γ , in Eq. (2). The color balance values, b_i , used throughout this study are 1.54, 1 and 2.45 for red, green, and blue channels respectively and were set using the camera software and Passport 2 ColorChecker (CCPPV2, Calibrite) under the same illumination conditions as the wafers to give an accurate depiction of the interference colors in the produced video. Due to the assurance of linearity by removing Γ , these values can be easily changed after capture as they represent scalars of the channel response.

2.1.2. Specular laser reflection

A 520 nm laser (Thorlabs, PL203) and large area photodiode are also mounted above the spin coater, perpendicular to the LED and camera, so that the laser reflects at 30° off the center of rotation onto the photodiode. The intensity of the reflected beam shows sequential peaks and can be interpreted as thinning by a length of $\lambda/2n\cos(\theta_1)$, where λ is the laser wavelength, n is the refractive index of the fluid and θ_1 is the angle of light propagation in the fluid (angle of refraction), found by Snell's law. This constraint denotes where the optical path difference (OPD) between the reflection from the top of the film and the substrate is equal to the wavelength of the light to produce points of constructive interference. When only solvent is used, and the final thickness is zero, this relation gives a centre-point thickness profile by counting peaks backwards. This has been a widely used technique employed in many previous studies [17,18,26] to impart center point thickness profiles. Fig. 6 shows the two simultaneously performed techniques, stroboscopic color

imaging and laser specular reflection, and how they are used to produce an *in-situ* color-to-thickness relationship.

In an industrial setting the footprint of this metrology setup could be reduced by carrying out the imaging at normal and laser reflectance at near-normal incidence, through a hole in the diffuser screen. This would provide a system that may only need a single mount directly above the wafer, thus making it much more modular. The drawback of this is that the reflection of camera lens, photodiode and laser source is likely to be visible in the center of the wafer and will limit analysis in the area that it occupies. Here, this configuration was not implemented because a larger instrument footprint was acceptable and imaging at 20° resulted in the etched glass diffuser occupying the whole area of the wafer. The postulated normal incidence system would, however, be likely to be marginally more accurate due to the optical path difference of a given thickness change being maximized.

2.2. Experiments

The viewpoint of the camera was corrected using NI Vision's grid calibration method to remove the perspective of the non-normal incidence. This uses an image of a 10×10 mm grid at the camera's viewing angle to fit a polynomial distortion model that then re-interpolates images so that the grid appears regular. This process means that raw images of oval wafers (due to camera angle) can be corrected so that the wafers appear circular. This process also accounts for any distortion due to the lens and sensor misalignment, which here is negligible compared

to viewing angle. The process comes with a mean error of 0.048 mm (approx. 1 pixel), and a standard deviation error of 0.00094 mm (approx. 1/100 pixel) with the edge regions of images having a higher error, additional information is found in supplementary information S7.

Substrates were test grade 3" diameter CZ grown (100) Si wafers, or cleaved sections of these wafers, from International Wafer Service. All were rinsed with isopropyl alcohol (IPA) and dried with compressed N₂ or cleaned with CO₂ snow [35] before mounting. The first run with all wafers was completed without the addition of solvent and was used to collect reference flat field images whilst under the same rotation and lighting conditions as subsequent runs. The selected solvent was pipetted onto the wafer until the wafer appeared completely flooded (typically 2 ml). Wafers were spun at 2500 rpm (full wafer) or 2000 rpm (20×20 mm squares), with an acceleration of 1500rpm/s, until complete evaporation occurred. Each experimental configuration was replicated 5 times on the same substrate and showed high levels of reproducibility. Typically, each sample was complete within 10–15 s.

2.3. Color to thickness mapping procedure

The pixels in each frame of the RGB images are software binned to find a mean RGB color for each bin (2×2). A suitable level of binning should reduce the effect of pixel noise, ϵ_i , without excessively reducing the resolution of the produced thickness maps. To determine how the level of binning affected the variance of the RGB color, and thus the final recovered thickness accuracy, a study was conducted on one of the stroboscopic videos, the details are presented in the supplementary information (S8). The standard deviation of color value was shown to be inversely proportional to the square bin width. This data was then used to inform the amount of tolerance in the color matching procedure. color matching of each channel to two standard deviations is used. For 2×2 binned videos this means the tolerances are set to 2.58, 1.61 and 2.14 for red, green, and blue channels respectively.

Each bin in the video is then matched to the *in-situ* color-thickness relationship, an example for which is shown for xylene spun at 2500 rpm in Fig. 3d, to solve for thickness. Due to the one-to-many matching of color to thickness, each bin may have more than one, or no, possible thicknesses assigned at this stage. All thickness solutions are found for each (x, y) bin over time. The time points that have single solutions are filled in, and a linear regression model is fit to these. This model was constrained to have a negative gradient (thinning through time is assumed). For time points with multiple solutions, the closest point to the model at each time is selected, as long as this point is reasonably close to the model (within 250 nm). This process does not aim to model the thinning, but uses the model as a tool to correctly identify the most likely correct thickness solutions by implementing the assumption of thinning. Thinning behavior that deviates significantly from the model (i.e. nonlinear) is still conserved because the single closest solution from the pixel color is ultimately assigned, not the model value. In the results produced in this paper, a linear model was able to accurately resolve the ambiguities because thinning below 2 μ m is approximately linear. In addition, multiple solutions are typically spaced far enough apart for resolution in this way due to the nature of the color signals. Polynomial and logarithmic models were also tested, however a significant improvement was not seen. Using a nonlinear model and constraining the fit parameters to reflect assumptions such as constant thinning may give better performance in solutions with very nonlinear thinning behaviors.

Next, any thicknesses that may have been incorrectly assigned must be identified and removed. This is an important step as in some cases the ambiguities may have led to incorrect solutions having been identified. This is achieved here by median filter thresholding. Each frame in the video is median filtered with a kernel and compared with the original frame. Values that differ by more than a threshold amount are very different from the surrounding neighbors and are therefore likely to be incorrectly assigned to thicknesses that violate the topology of the fluid;

these thicknesses are identified and removed. A kernel size of 15×15 bins (1.82 mm²) and a threshold of 75 nm was chosen. The result of this process is that bins that differ by greater than 75 nm of the median of the surrounding area are identified and removed.

Bins that are not assigned thicknesses are then assigned using a purpose-built iterative linear interpolator in x, y and t dimensions. This method was chosen as the time for computation scales much more slowly than out-of-the-box alternatives that employ more computationally expensive procedures. In addition, the custom-built function could take advantage of multiprocessing to further speed up the process. The error of the interpolation and the time demand for different numbers of points is shown in the supplementary information (S9). The computational demand of interpolation is an important consideration in this application when there may be over 1×10^8 bins in each video. Out-of-the-box interpolators struggle to deal with matrices of this size within a realistic time frame.

The linear interpolation is expected to give satisfactory results as it maintains realistic topology of the fluid in x, y and t, however, if large areas of unassigned pixels are present, especially if these fall at the edge of the matrix, topological features may be obscured or misrepresented. Care should be taken when using this method to assess small length scale features such as defects, in areas that are sparsely populated with color-to-thickness solutions, such as the band in Fig. 7b which occurs at very high fluid gradient. These areas are still small enough (less than 10 pixels, under 0.5 mm) that the assumption of linear fluid profile holds well. In cases such as this, the particular thickness range may not be well described by the color-to-thickness relationship and therefore thickness solutions cannot be found, this may be because the gradient is so steep that the pixel becomes an average of many colors/thicknesses to produce a color that is not well described by the developed color-to-thickness solution.

The mapping procedure relies on the underlying assumption that the color changes observed in the center of rotation can be applied to all areas on the wafer. The diffuser in place between the LEDs and the spin coater, combined with the flat field correction of the images, ensure that this is satisfied. In addition, there is an assumption inherent in the processing steps that for most points the thickness is correctly identified at the initial stage. This is found to be a reasonable assumption for the systems studied and the matching tolerances used. The number of points that have been assigned or removed at each stage in the processing is summarized in Table 1. This shows that the number of pixels changed at each stage in the procedure.

3. Results and discussion

3.1. Full wafer

The full wafer thickness reconstructions clearly capture the bulk thinning behavior of the solvent as evaporation occurs. This can be seen in the 3D renderings in Fig. 8. The thicker portion at the edge of each wafer due to the beading effect of the xylene, that was seen in the stroboscopic images in Fig. 3, is also clearly visible. In addition to this, smaller scale thickness variation effects caused by imperfections or defects can be observed evolving over time with this technique. Their presence is further confirmation of the ability of this set-up to freeze the rotating image, revealing high lateral resolution. Fig. 9 shows example frames of the supplementary information (S10–S12) resultant animated heatmaps for each run configuration, also played back at 15fps. Representative frames at ~300 ms before drying have been chosen that correspond with the frames in Figs. 4 and 5.

The processed videos and thickness maps reveal that, for spun coat xylene, an edge bead is clearly visible throughout the drying process, however, the bulk of the wafer remains at a uniform thickness value. In the data from butyl acetate, this beading is not present and the thickness across the wafer is uniform up until the very edge. In both videos, comet defects are present due to foreign objects on the wafer, and these have

Table 1

The percentage of found or removed pixels at each stage of the processing, reported as $\mu \pm \sigma$ for five runs.

Solvent	Substrate	color-thickness matches (%)	Filled by assumption (%)	Values removed (%)	Pixels 3D interpolated (%)
Xylene	3" Si wafer	83.02 \pm 2.95	15.77 \pm 2.82	-2.65 \pm 0.39	3.86 \pm 0.61
Butyl acetate	20 \times 20 mm Si section	85.21 \pm 1.35	14.00 \pm 1.28	-2.05 \pm 0.73	2.84 \pm 0.46
Xylene	3" Si wafer	40.90 \pm 5.26	44.21 \pm 4.55	-12.46 \pm 2.52	27.34 \pm 3.12

been preserved well in the mapping to thickness, maintaining a high resolution and clear thickness variations due to disturbance in the fluid flow around them. The examples in Fig. 5g and h show that the defect largely maintains a constant relative disturbance up until the drying point. In a cross section perpendicular to the radial flow, the profile of the disturbance caused is a "w" shape and is roughly 100 nm from peak to trough.

Fig. 10 displays the vertical line profile through the center point of the wafer at 100 ms intervals relative to the drying time. 5 mm sections from the center and the edge of the wafer are shown and the rest of the data is omitted for readability. The thickness between frames has been interpolated here to provide profiles at uniformly spaced time points. The spacing of the lines indicate the rate of thinning and this is largely uniform for each point on the wafer, excluding the xylene edge bead. As expected from the relative vapor pressures of the solvents the rate of evaporation of butyl acetate was faster than that of xylene.

The difference in evaporation rate of the solvents is further apparent from the frame thickness distributions, shown in Fig. 11. These show data on the number of pixels at each thickness value for every frame in the drying video. The "nominal" thickness on the wafer is represented by the diagonal high intensity band, with the gradient of the band representing nominal film drying rate. Variations in thickness from this are seen in the areas of lower and higher frequency around it, colored as a light blue band.

The thickness variation above the nominal thickness of xylene persists from -2000 ms to 0 ms (the center drying point), this is consistent with the observations of a significant edge bead in the images. The maximum height of the edge bead reduces from 0.62 μ m above the nominal height of 1.28 μ m at -2000 ms to 0.36 μ m above the nominal height of 0 μ m at the point of drying (0ms). This shows that the edge bead is thinning faster than the bulk of the wafer but suggests that this is not due to a difference in evaporation rate at different radii, because of the high uniformity at all other points on the wafer. This phenomenon reduces the magnitude of the edge effect closer to the drying point. In contrast, the same data collected for butyl acetate has a much smaller variation in thickness throughout the observed drying, suggesting that here the drying rate is uniform.

It is clear from Fig. 7a that the edge bead of xylene has already formed over 2 s before the drying point, at a nominal fluid thickness of around 1.25 μ m, suggesting that the edge bead was present from early in the spinning regime, forming during hydrodynamic thinning. Whilst extrapolation thickness variations to earlier time is limited by RGB similarities at this thickness, this edge can be discerned at larger thicknesses qualitatively in the images due to the difference in intensity that it creates. Xylene has a higher surface tension and viscosity when compared to butyl acetate; both solvent properties play a crucial role in the solvent uniformity. The edge bead forms because the xylene can spread less easily over the surface of the wafer due to centrifugal forces and is more likely to form a bead before being ejected from the edge of the wafer due to its high surface tension.

3.2. Non-axisymmetric (square) wafer

Spin coating runs were also conducted on cleaved silicon wafer (20 \times 20 mm), spun at 2000 rpm with xylene. The same type of edge effect that is observed on the full wafer is also observed here, where there is significant beading of the solvent that is visible from 2 μ m and is therefore likely first formed in the hydrodynamic thinning regime. In

Fig. 12, additional effects due to the wafer geometry can be seen. The drying of the solvent outside of the non-radially symmetric sections of the wafer are much slower than at the center.

3.3. Length scale discussion

Stroboscopic illumination with LEDs allows for the effective sensor integration time to be controlled well below the minimum shutter times of most cameras. The minimum effective exposure time possible is then only constrained by the rise and fall times of the LEDs, typically in the tens of nanoseconds range [34]. Or, when operating at very small pulse lengths, the intensity of illumination becomes limiting to generate sufficient activation of the sensor with an acceptable signal to noise ratio.

A shorter strobe illumination time results in a smaller length of travel of the moving object, in this case a rotating substrate, during the exposure and a more effective freezing effect. As the radius or the rotational frequency of the substrate increases so does the tangential velocity, requiring shorter and shorter strobe flashes to achieve the same level of detail in the image. The length of the strobe illumination that allows a movement of distance l by an object rotating at ω rpm with a radius r , is given by Δt in Eq. (3).

$$\Delta t = \frac{l}{2\pi r \left(\frac{\omega}{60}\right)} \quad (3)$$

During the digital imaging of a moving subject, a clear image may be formed by accepting movement of no more than the real-world length of 1 pixel. Fig. 13a shows the maximum strobe pulse times needed to freeze an image in this way. In this scenario, the limit of length scale that can be examined is set by the resolution of the camera rather than the blur created by travel during the strobe pulse. This constraint may be relaxed as the observational length scale needed changes to lengths beyond the resolution of the camera. This may also increase the quality of the photos by ensuring sufficient illumination. Extremely short illumination pulses, even with bright LEDs, run the risk of under illuminating the wafer. This increases the need for large gain, reducing the dynamic range of the resulting images.

In this study, wafers of a maximum radius of 38.1 mm were spun at 2500 rpm. At these conditions the strobe pulse length required is 4.51 μ s to achieve the pixel-scale freezing described above at the circumference. The strobe pulse used in this study is 30 μ s and is selected to give the most effective trade-off between amount of illumination and image blur. A pulse of 30 μ s is 6.65 times longer than the maximum calculated; this is an important ratio and will give the number of pixels traveled across by a point at the edge of the 3" diameter wafer during the strobe, resulting in a blur length of 299 μ m. Any metrology at this radius is constrained to the length of 7 pixels (315 μ m), however, this minimum length scale decreases linearly to just 1 pixel (45 μ m) at the center. Here, this level of blurring in the images is minimal, as to be essentially imperceptible in the raw and processed videos. In the resulting heatmaps, where the pixels have been binned by 2 in each direction, this resolution has been halved. This reduction in resolution can be mitigated by increasing the pixel density of the system by either using a higher resolution camera, modifying the geometry of the setup so that the wafer occupies a larger ROI in the existing camera, or with use of a higher magnification lens (at the expense of FOV).

Since 2001, 300 mm (18") wafers have been used in the semiconductor industry. For spin speeds of 2000 rpm this would require a

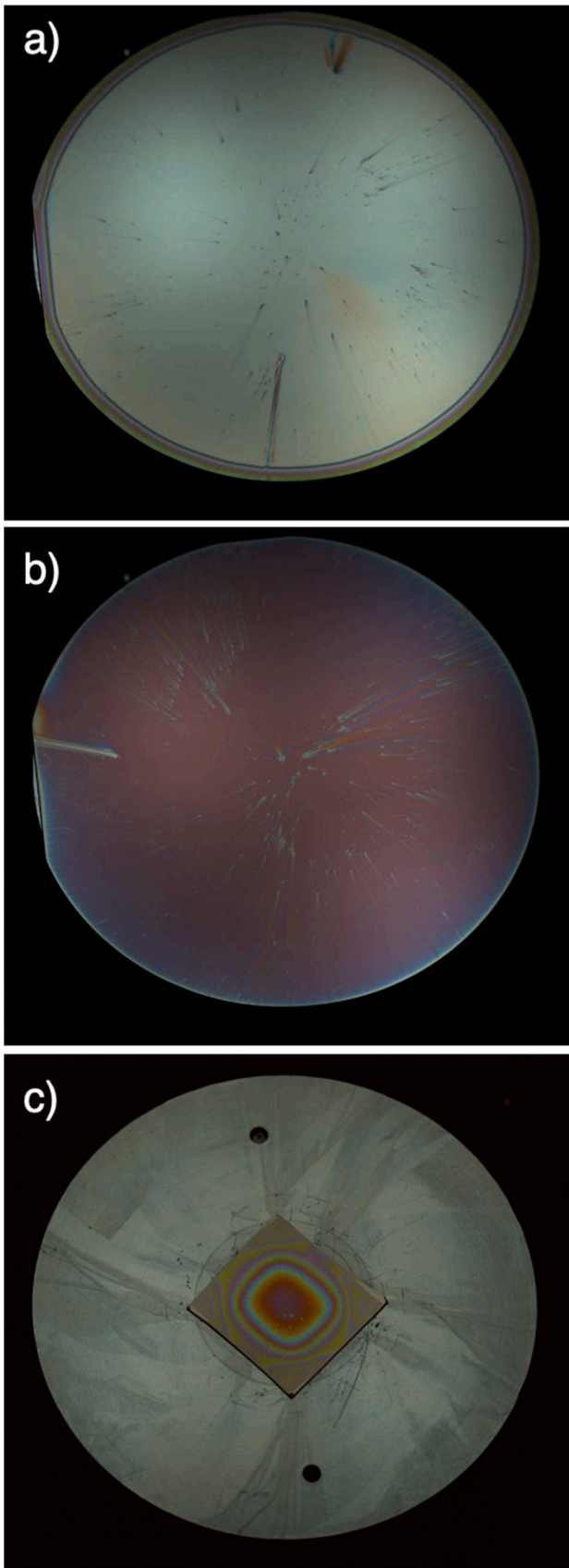


Fig. 4. Stills of the raw videos from (a) S1 xylene spun at 2500 rpm on a full 3" wafer (b) S2 butyl acetate spun at 2500 rpm on a full 3" wafer and (c) S3 xylene spun at 2000 rpm on a 20×20 mm cleaved section of wafer, all taken roughly 300 ms before drying occurred.

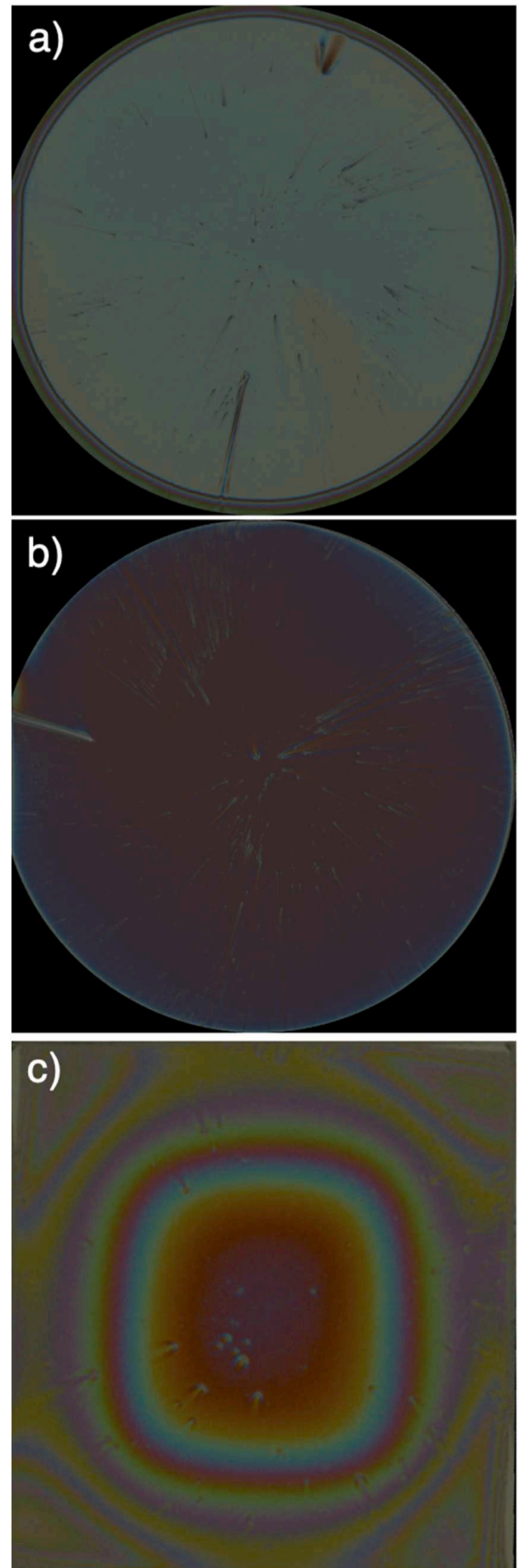


Fig. 5. Stills from the processed videos (a) S4 xylene spun at 2500 rpm on a full 3" wafer (b) S5 butyl acetate spun at 2500 rpm on a full 3" wafer and (c) S6 xylene spun at 2000 rpm on a 20×20 mm cleaved section of wafer, all taken roughly 300 ms before drying occurred.

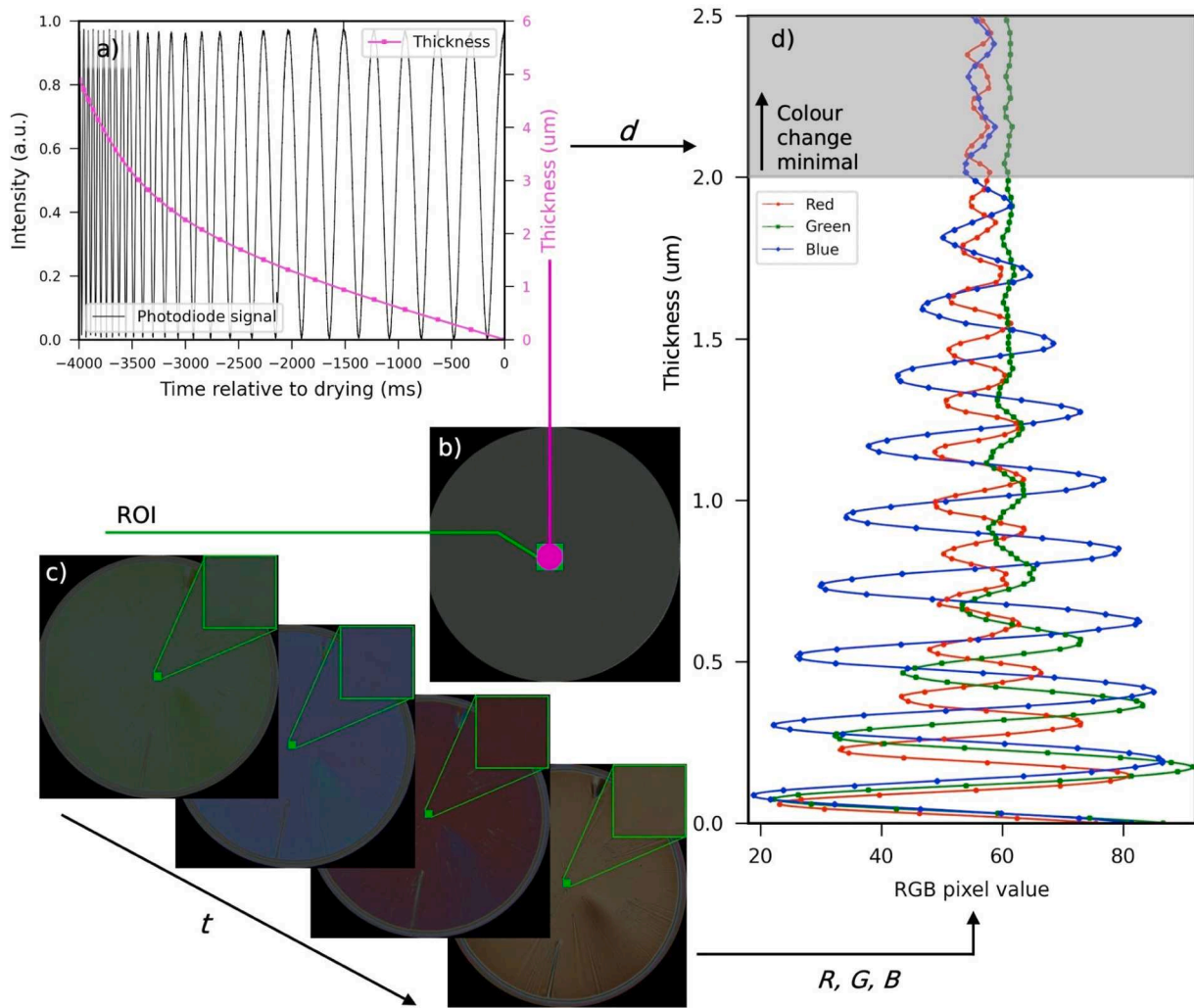


Fig. 6. (a) The specular reflection intensity (black) and the centre point thickness profile obtained by resolving the Bragg condition (magenta); (b) A schematic of the wafers surface and the 9×9 pixel $403 \times 398 \mu\text{m}$ laser spot (magenta circle) and overlapping ROI (not to scale) for the RGB color extraction (green square); (c) The centre RGB values being extracted from each frame; (d) the *in-situ* color-thickness relationship developed from the combination of white light imaging and laser specular reflection data, the grayed out area shows where the color differences become hard to distinguish.

strobe pulse of $9.52 \mu\text{s}$ to be imaged at the same level of blur discussed here (or a pulse of $1.43 \mu\text{s}$ to achieve complete pixel level freezing, with the same camera resolution). This is achievable with modern LEDs as their small size means many high-powered modules can be packed into small arrays to illuminate the surface of the wafer, even in short times.

Another important trade-off considered is the frame rate and resolution of the camera used. Not only does the resolution affect the maximum length scale observable, but in many cameras the ROI size (and therefore the resolution) will affect the maximum achievable framerate. The possible frame rate must be sufficiently high to at least match the number of revolutions per second of the spin coater to achieve a frame every rotation. Above this, it would be possible to run the setup so that an image was achieved every two or three rotations of the substrate, however, especially with quicker drying solvents, this will potentially reduce the number of points in the color-to-thickness relationship so that it cannot be reliably constructed.

3.4. Recovered thickness accuracy discussion

The accuracy of the center thickness profiles resulting from the laser specular reflection can be checked using a Meyerhofer plot [36,37]. This used the Meyerhofer model [16] of a spun coat fluid, presented in Eq.

$$(4), \text{ where } K = \frac{\rho\omega^2}{3\eta}.$$

$$\frac{dh}{dt} = -2Kh^3 - e \tag{4}$$

By comparing the value of K resulting from literature values of viscosity and density to the value of K calculated from the slope of the linear regression plot of $-\frac{dh}{dt}$ against $2h^3$. The center point thickness profile's fit to the Meyerhofer model can be evaluated. Here, for each run configuration, the 95 % confidence interval of the slope of the plots contained the literature reported K values. This gives good confidence that the specular laser reflection thickness values at the center of the wafer are accurate.

The effect of thicker films satisfying constructive/destructive interferences for a broader range of wavelengths gives an upper limit to this approach, as seen in the RGB color signals in Fig. 3d. The origin of this dampening of the interference colors is due to the integration on the camera's sensor. As film thickness increases, so does the frequency of the reflectance wave, and the relative activation across the red, green, and blue bands in the Bayer filter becomes more even. Eventually, at high thicknesses, the intensity variation in a single channel becomes much less dependent on thickness, and the color of the bulk material emerges. This enveloping phenomenon is not present in the laser data because the

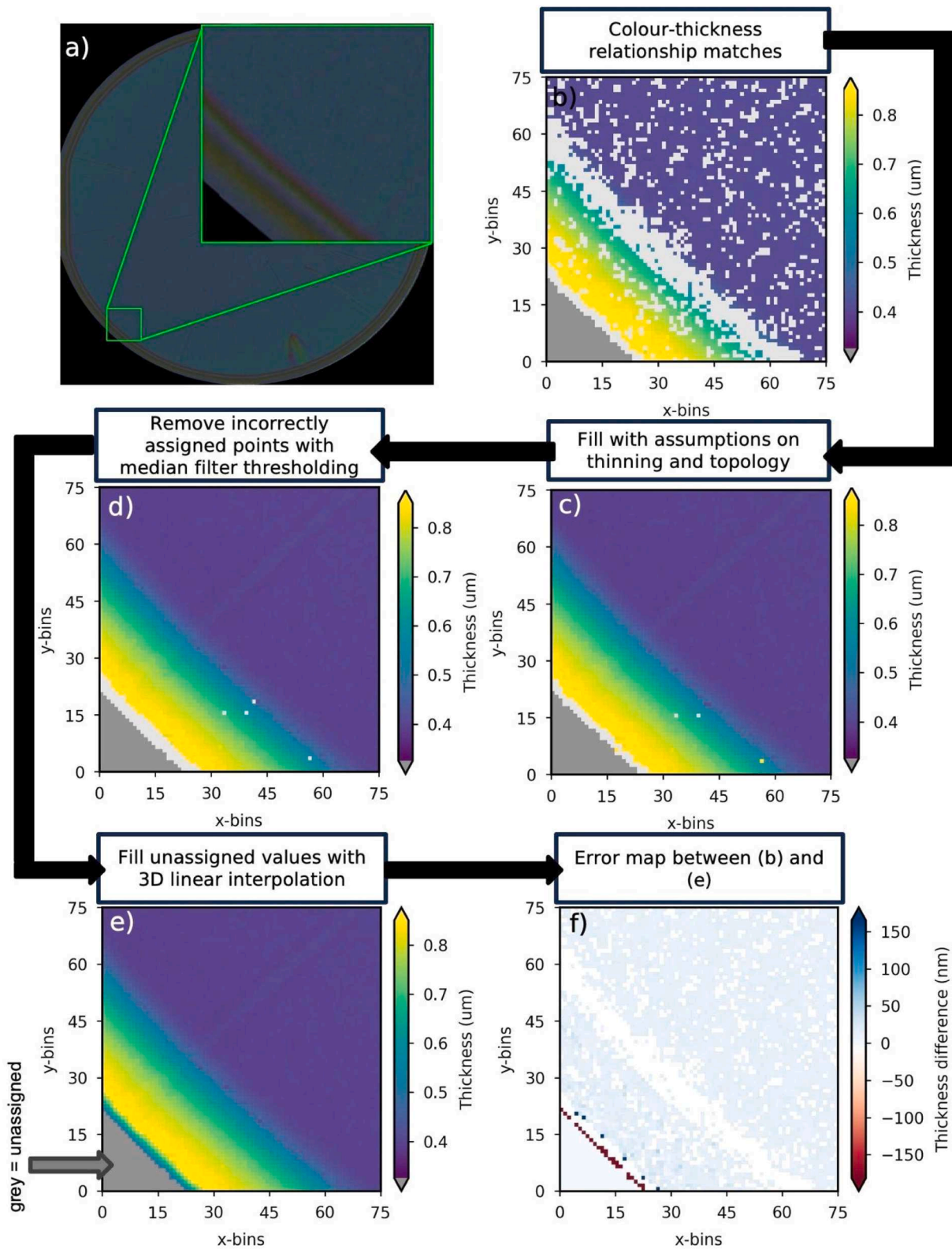


Fig. 7. A representation of the processing steps taken to produce the final thickness profiles, shown on a 75x75 bin Section of a video frame from the bottom left of the full frame at the wafers edge. (a) the image of the wafer with the ROI annotated (b) the initial color to thickness matched values (c) filled using assumption of thinning and surrounding pixel values (d) removal of incorrectly assigned points, e.g. bin (56,4) via median filter thresholding (e) 3D interpolation of any further missing points (f) error from (b) minus (e), where both points exist.

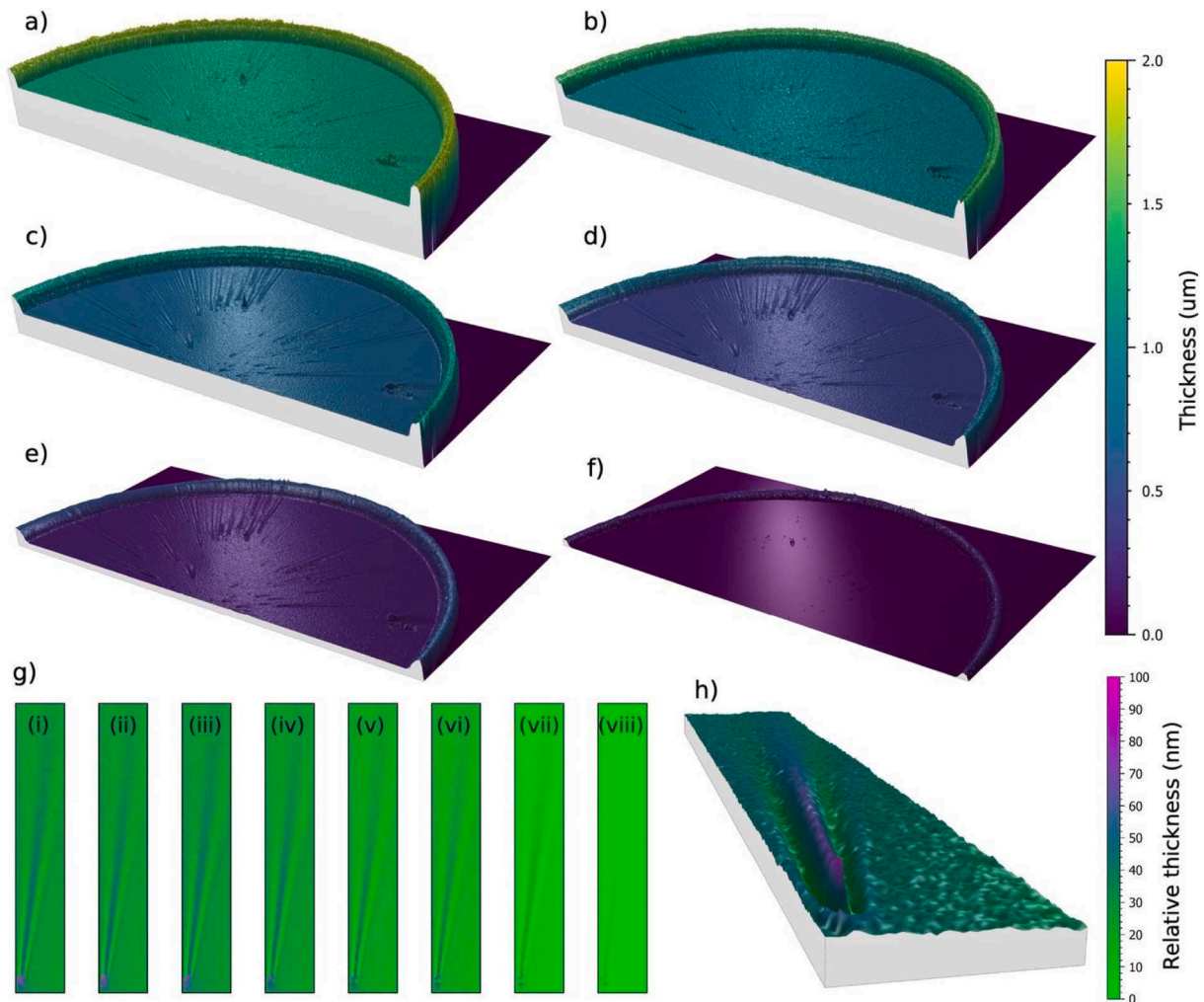


Fig. 8. Half wafer thickness renders of xylene spun coat at 2500 rpm, taken from times (a) -1951 ms (b) -1541 ms (c) -1132 ms (d) -723 ms (e) -313 ms (f) 96 ms relative to center point drying; (gi-viii) relative thickness maps of a 30×3.45 mm section of the wafer containing a comet defect close to drying, at -169 , -144 , -120 , -96 , -72 , -48 , -24 and 0 ms respectively; (h) a relative thickness rendering of the comet defect at -1132 ms.

photodiode is only logging activation. The impact of this effect is that for films of $n \approx 1.5$ and $k \approx 0$ on silicon, the maximum thickness that can be resolved by color analysis is around $2\mu\text{m}$. If the thickness is greater than this, the optical interference is not pronounced enough to interpret as a color difference in a digital image. It is not possible to reduce this enveloping effect with camera settings and thus this thickness limit is fundamental to the technique.

A significant result of this enveloping phenomena is that the matching procedure, that uses a constant tolerance for each channel, changes accuracy at different thicknesses. In general, it is more accurate at lower thicknesses because the frequency, and therefore gradient, of the color response is higher which results in a smaller matched thickness range. The tolerances in the matching procedure have been selected to be representative of the variance present in the color measurements to minimize the error, further details of this are available in the supplementary information. For example, for the data presented in Fig. 3, a blue channel value of 60 ± 2.14 will match to 16 thickness values. Thicknesses between 0.028 and $0.031\mu\text{m}$ at the thinnest solution, thicknesses between 0.889 and $0.895\mu\text{m}$ at the 8th thinnest solution, and between 1.660 and $1.676\mu\text{m}$ at the 16th thinnest solution. In situations such as this, where a range of values are identified on the 1 nm step interpolation of the color-to-thickness relationship, the mean of the range is taken as the solution. Matching all three color channels simultaneously narrows these matched ranges significantly.

Fig. 14a displays the number of solutions found for each pixel for the full wafer video of Xylene spun at 2500 rpm, as the color matching tolerance is changed between 0.5 and 3 times the identified color standard deviation (S8). If the color matching tolerance is too low, thickness solutions fail to be identified and a large number of pixels with no solution are present, however, if the tolerance is too large, the number of pixels with multiple solutions increases, in turn increasing the amount of ambiguities that need to be resolved. Fig. 14b shows how these different matching tolerances affect the error in the thickness solutions by identifying the range of color, and therefore thicknesses, within the tolerance at each solution. Setting the matching tolerance too high results in larger potential percentage errors because the matched color solution can be more different from the pixel color, and therefore further away from the true thickness. The figure also demonstrates an additional reason why thickness estimation beyond $2\mu\text{m}$ is not recommended, as the enveloping of the signal drastically increases the potential matched thickness error. Matching to two standard deviations of color is chosen as it provides a satisfactory trade off in maximizing single solution pixels while keeping these errors low.

Finally, Fig. 14c displays the percentage error at the matching tolerance used (2 standard deviations of color) overlaid onto the developed color-to-thickness relationship. This shows that increases in the error of the matching correlate with the combined steepness of the color responses, a result of using a constant matching tolerance, because

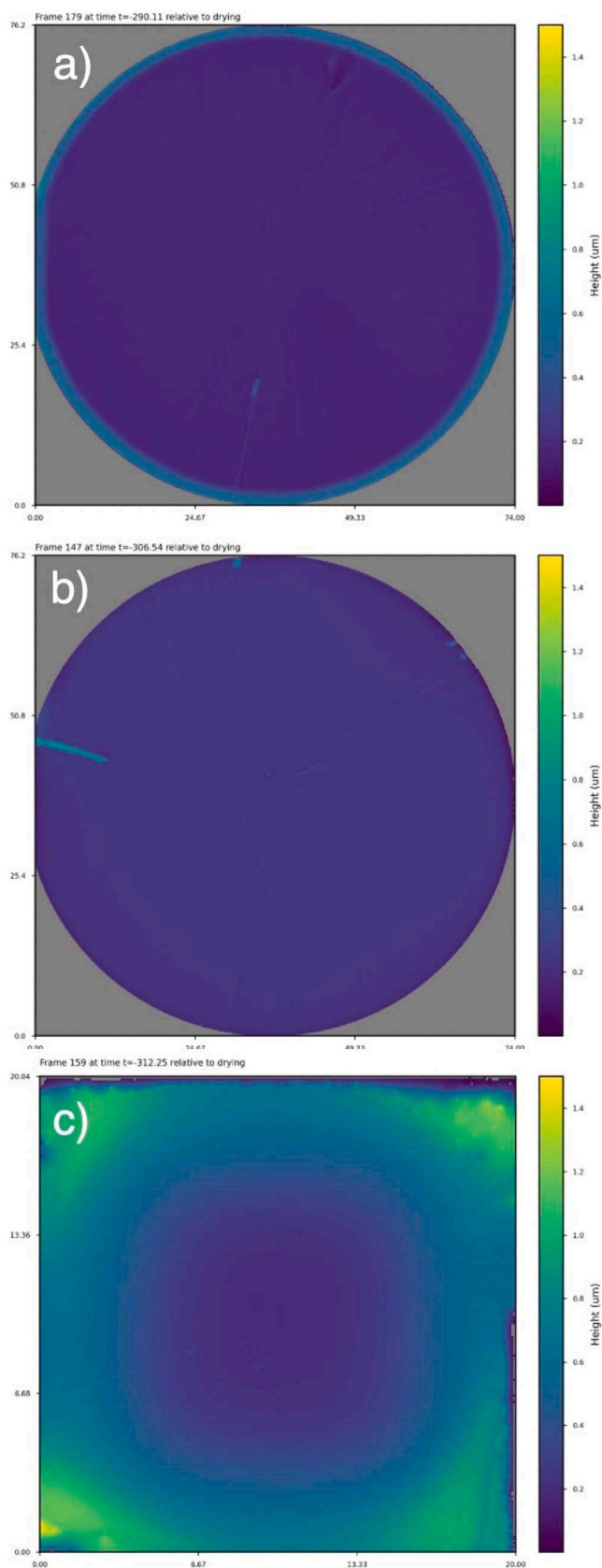


Fig. 9. Stills from the animated heatmaps (a) S9 xylene spun at 2500 rpm on a full 3" wafer (b) S10 butyl acetate spun at 2500 rpm on a full 3" wafer and (c) S11 xylene spun at 2000 rpm on a 20×20 mm cleaved section of wafer, all taken roughly 300 ms before drying occurred.

a larger range of colors and therefore thicknesses are matched. Despite this, these errors stay below 5 % of the thickness value for almost all the points, apart from extremely low thickness values less than 100 nm.

4. Conclusion

In-situ stroboscopic white light imaging of a spun coat wafer has been demonstrated over areas of up to 45 cm², making this the largest area imaging study of the spin coating process of its kind. The developed metrology technique has been used to produce thickness maps of solvents spun coat on silicon, in addition to full high resolution RGB videos of the process. To successfully achieve this technique, a trade-off between camera resolution, spin speed and strobe pulse length has been found and the interplay of these has been discussed.

Thickness can be resolved at any point on the wafers surface between the development of interference colors at around 2µm. The resolution and error of these thicknesses is difficult to quantify due to the nature of the reconstruction procedure, however, we find that the error in the matching procedures thickness values is less than 5 %. The use of broadband white LEDs for high illumination intensity has made this technique widely accessible. Moreover, the issue of color-to-thickness ambiguity, which arises from this approach, has been demonstrated to be resolvable through the application of basic assumptions regarding the film's topology. This technique involves very little a-priori information, limited to just the refractive index of the solvent at the laser wavelength. The Bayer filter sensitivity and illumination spectrum of the imaging is not required because the color-to-thickness relationship is constructed *in-situ*. This also means that this technique can be applied where fully controlled environments are not available.

In this study we have drawn light on how the physical properties of solvents affect the uniformity over whole-wafer areas. The experiments directly reveal that the evaporation rate of the solvent is uniform over the wafer's surface if the solvent enters the evaporation dominated stages of the process with a uniform profile. However, if an uneven fluid surface is present when entering this stage, then an irregular evaporation rate is observed over the wafer. In this scenario, the evaporation rate of the thicker areas is slightly larger, decreasing the scale of the nonuniformity as the spin-coating progresses. Reasons for entering the evaporation dominated stages with a nonuniform thickness across the wafer may include a high surface tension, high viscosity, or extremely fast evaporation due to a high vapor pressure but is likely to be a complex result of all three of these solvent properties, as well as any effects from non-axisymmetric wafer geometry.

4.1. Future work

This work can be extended to directly observe the formation of films with a final thickness that is not zero i.e. spun coat solutions rather than pure solvents. This would require the *ex-situ* measurement of the film at the center of rotation with a technique such as SE.

Due to the recent advances in hyperspectral camera technology, that brings framerates in line with that needed, snapshot hyperspectral cameras could be used to resolve thickness unambiguously, such as in the work by Chandran Suja et al., albeit at an order of magnitude increased cost in terms of \$, and an order of magnitude reduction in pixel resolution. To combat this reduction in resolution, simultaneous hyperspectral and normal digital imaging poses a good solution that can be used to maintain resolutions currently unavailable in snapshot hyperspectral imaging systems.

Methods to estimate spectra from RGB color triplet have been described in literature [38]. Successful application of these methods would allow the reflectance spectrum to be estimated directly from the imaging data, but doing this accurately is a major challenge. This could then be coupled with existing thin-film reflectometry methods [39,40] to define a thickness. With proper calibration, this would mitigate the need for the laser specular reflection described here, and the thicknesses

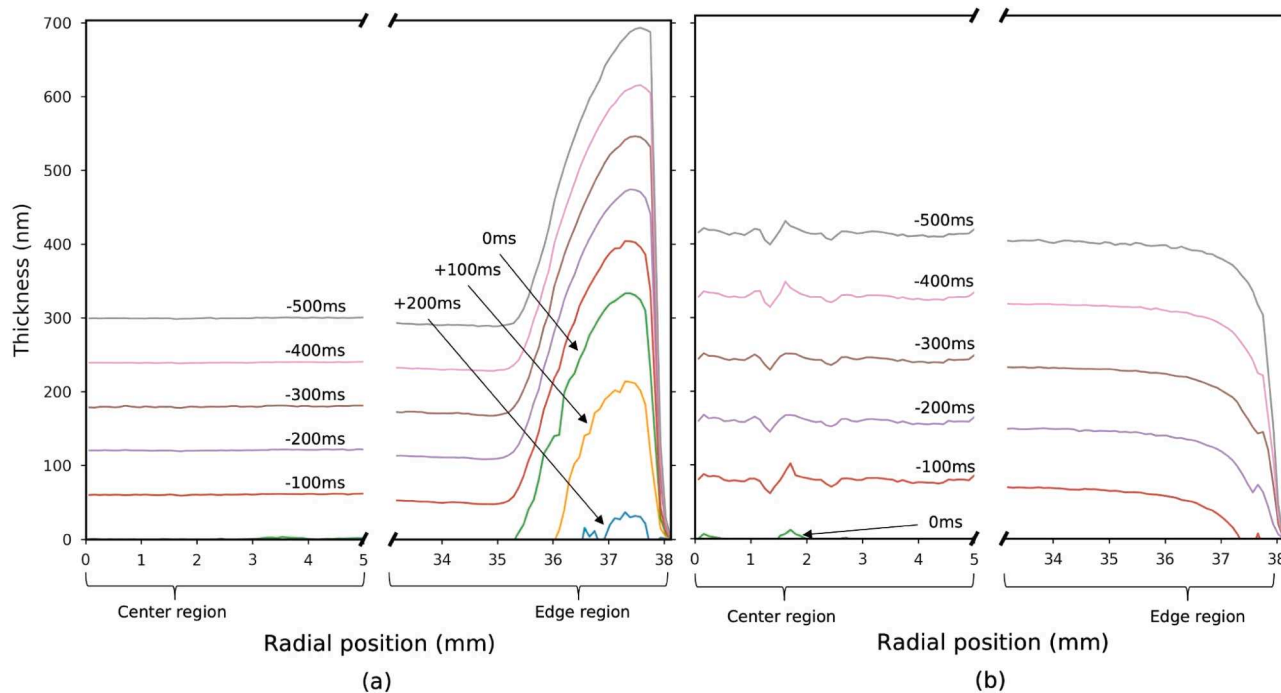


Fig. 10. The thickness of a vertical line profile through the center point of a wafer at specific times relative to the center point drying for (a) xylene and (b) butyl acetate spun at 2500 rpm (positive time legends shown in (a), left indicate drying times after the center of the wave has fully dried).

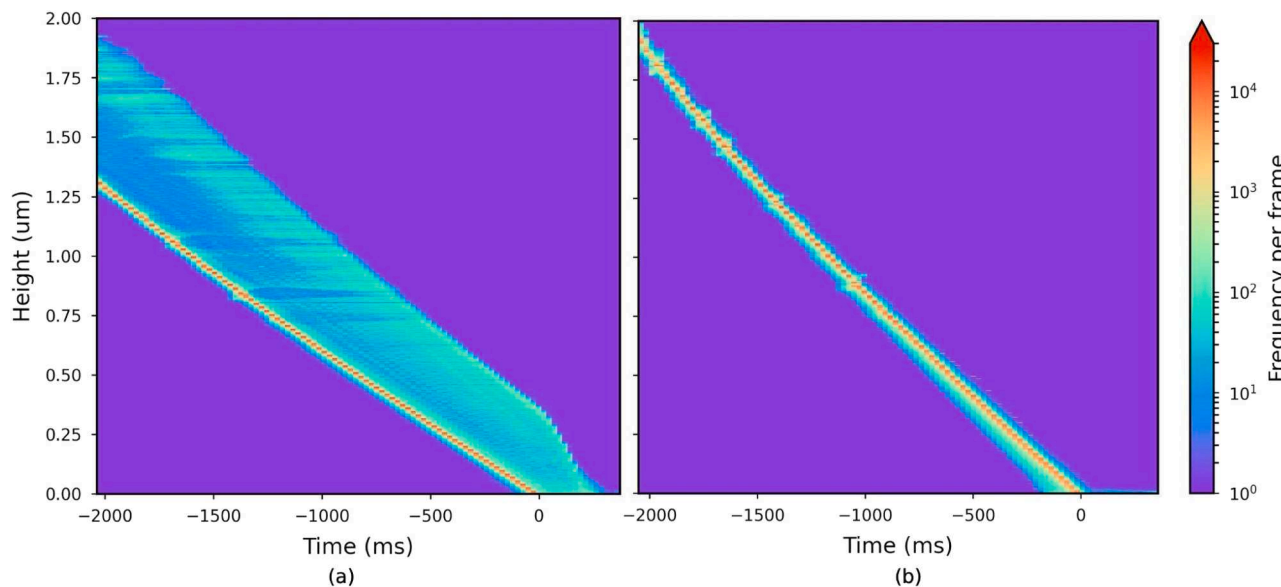


Fig. 11. Horizontally stacked histograms for each frame quarter (upper left quadrant) where the frequency of each thickness is shown by color in a log scale, for (a) xylene and (b) butyl acetate spun at 2500rpm. These histograms are limited to regions below 2 μ m where colors can be clearly identified, for both solvents this is around 2 s from drying, despite the differences in vapor pressure, due to xylene’s edge bead.

of spun coat solvents or solutions could be identified from just the stroboscopic images. Challenges to these approaches include that these methods can require lots of data about the imaging system or require training data consisting of reflectance spectrum and camera response pairs, or both.

Funding sources

This research did not receive any specific grant from funding agencies in the public, commercial, or not-for-profit sectors.

CRediT authorship contribution statement

Jack B.P. Atkinson: Writing – original draft, Visualization, Software, Methodology, Investigation, Formal analysis, Data curation.
Jonathan R. Howse: Writing – review & editing, Validation, Supervision, Resources, Project administration, Methodology, Funding acquisition, Conceptualization.

Declaration of competing interest

The authors declare that they have no known competing financial

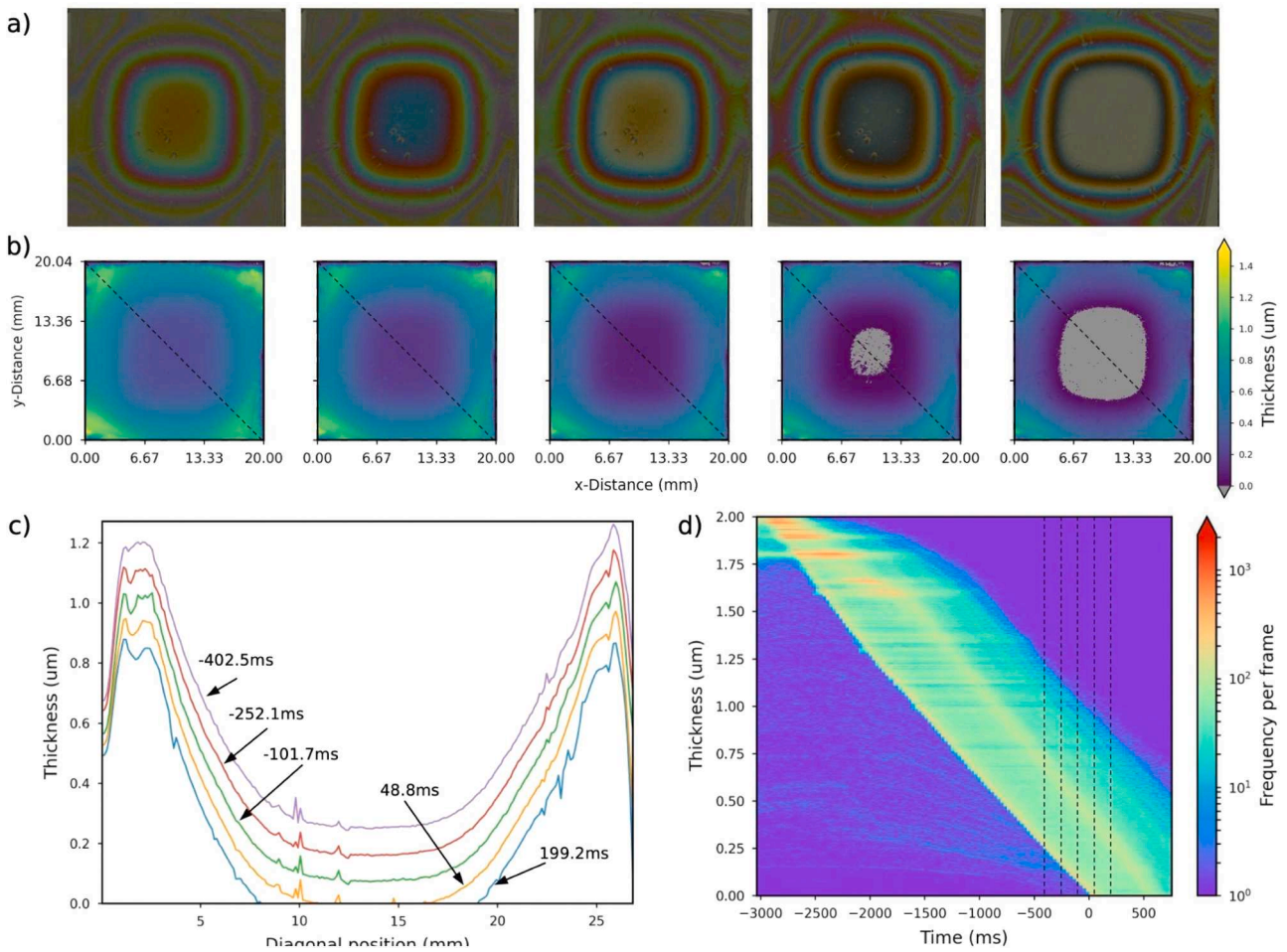


Fig. 12. (a) frames from the stroboscopic video of xylene spun on a 20×20 mm wafer at 2000 rpm, (b) the processed thickness heat maps corresponding to the frames in (a), (c) the diagonal line profiles of (b) annotated with the time relative to drying, and (d) the horizontally stacked histograms of the whole drying video, annotated with the timestamps of the frames in (a) and (b).

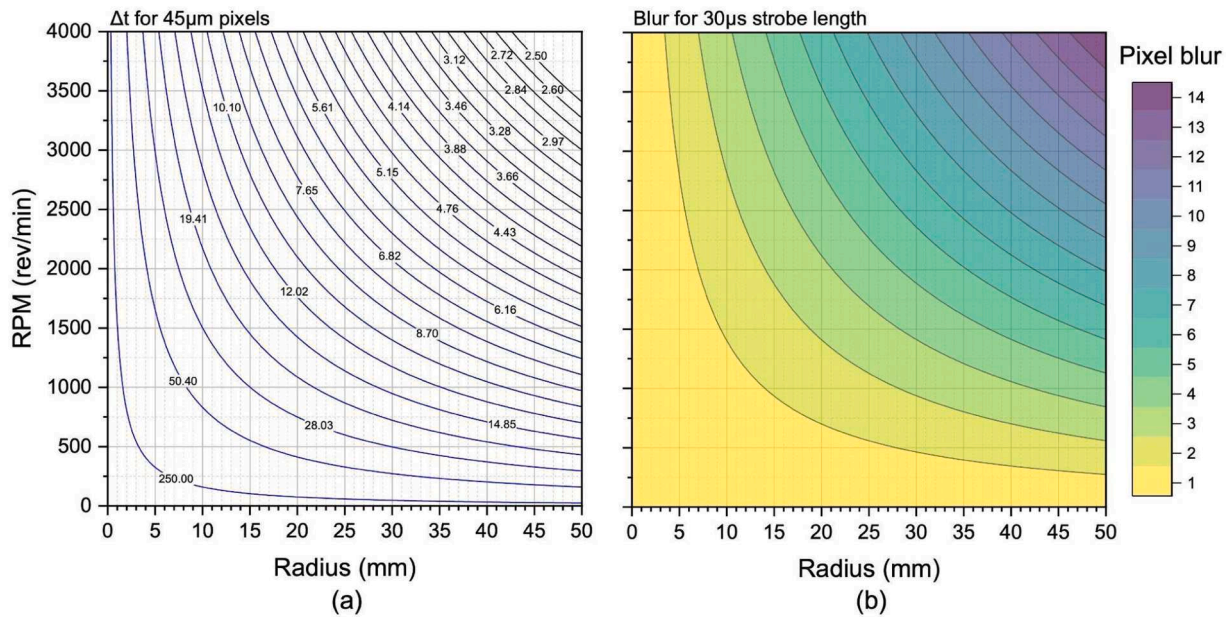


Fig. 13. (a) Contour plot showing the maximum strobe time in microseconds, from 250 to 2.5 in a reciprocal scale, required to freeze an image to one pixel length and (b) the amount of blur in number of pixels experienced at points for a 30 μs strobe flash.

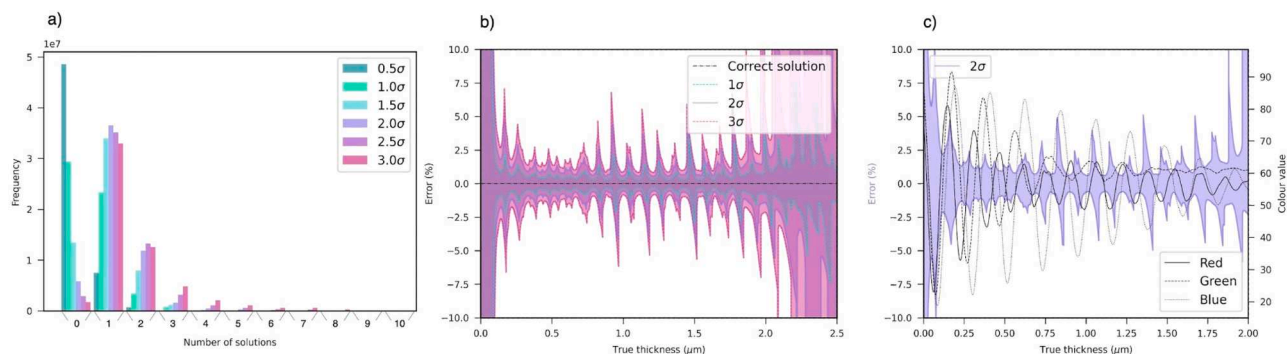


Fig. 14. (a) The number of solutions identified in the color-to-thickness relationship when the color matching tolerance is set to different levels of the camera color variance (b) the percentage error in thickness that results from matching to different levels of the camera color variance, and (c) the error given by the used color matching tolerance overlaid with the color-to-thickness relationship.

interests or personal relationships that could have appeared to influence the work reported in this paper.

Supplementary materials

Supplementary material associated with this article can be found, in the online version, at [doi:10.1016/j.optlaseng.2024.108692](https://doi.org/10.1016/j.optlaseng.2024.108692).

Data availability

Data will be made available on request.

References

- Kim SJ, Yoon S, Kim HJ. Review of solution-processed oxide thin-film transistors. *Jpn. J. Appl. Phys.* 2014;53. <https://doi.org/10.7567/JJAP.53.02BA02>.
- Matsui H, Takeda Y, Tokito S. Flexible and printed organic transistors: from materials to integrated circuits. *Org Electron* 2019;75(September):105432. <https://doi.org/10.1016/j.orgel.2019.105432>.
- Hu Z, Huang F, Cao Y. Layer-by-layer assembly of multilayer thin films for organic optoelectronic devices. *Small Methods* 2017;1(12):1–12. <https://doi.org/10.1002/smted.201700264>.
- Li C, Liu X, Du X, Yang T, Li Q, Jin L. Preparation and optical properties of nanostructure thin films. *Appl Nanosci* 2021;11(7):1967–76. <https://doi.org/10.1007/s13204-021-01930-4> (Switzerland).
- Wang XD, Li WG, Liao JF, Kuang DB. Recent advances in halide perovskite single-crystal thin films: fabrication methods and optoelectronic applications. *Sol RRL* 2019;3(4):1–27. <https://doi.org/10.1002/solr.201800294>.
- Zhao P, Xiong L, Li X, Guo Y, Xie Y, Du X. Research and application progress of conductive films in energy storage devices. *Adv Mater Technol* 2023;2300194: 1–23. <https://doi.org/10.1002/admt.202300194>.
- Chou LH, et al. Semiconducting small molecule/polymer blends for organic transistors. *Polymer* 2020;191(January):122208. <https://doi.org/10.1016/j.polymer.2020.122208> (Guildf).
- Xue L, Zhang J, Han Y. Phase separation induced ordered patterns in thin polymer blend films. *Prog Polym Sci* 2012;37(4):564–94. <https://doi.org/10.1016/j.progpolymsci.2011.09.001> (Oxford).
- Dalnoki-Veress K, Forrest JA, Stevens JR, Dutcher JR. Phase separation morphology of spin-coated polymer blend thin films. *Phys A Stat Mech Appl* 1997; 239(1–3):87–94. [https://doi.org/10.1016/S0378-4371\(96\)00471-2](https://doi.org/10.1016/S0378-4371(96)00471-2).
- Lee JH, et al. Effect of crystallization modes in TIPS-pentacene/insulating polymer blends on the gas sensing properties of organic field-effect transistors. *Sci Rep* 2019;9(1):1–9. <https://doi.org/10.1038/s41598-018-36652-1>.
- Jiang P, McFarland MJ. Large-scale fabrication of wafer-size colloidal crystals, macroporous polymers and nanocomposites by spin-coating. *J Am Chem Soc* 2004; 126(42):13778–86. <https://doi.org/10.1021/ja0470923>.
- Pichumani M, Bagheri P, Poduska KM, González-Viñas W, Yethiraj A. Dynamics, crystallization and structures in colloid spin coating. *Soft Matter* 2013;9(12): 3220–9. <https://doi.org/10.1039/c3sm27455a>.
- Toolan DTW, Fujii S, Ebbens SJ, Nakamura Y, Howse JR. On the mechanisms of colloidal self-assembly during spin-coating. *Soft Matter* 2014;10(44):8804–12. <https://doi.org/10.1039/c4sm01711k>.
- Zhang J, Li Y, Zhang X, Yang B. Colloidal self-assembly meets nanofabrication: from two-dimensional colloidal crystals to nanostructure arrays. *Adv Mater* 2010; 22(38):4249–69. <https://doi.org/10.1002/adma.201000755>.
- Wang T, et al. The development of nanoscale morphology in polymer:fullerene photovoltaic blends during solvent casting. *Soft Matter* 2010;6(17):4128–34. <https://doi.org/10.1039/c0sm00343c>.
- Meyerhofer D. Characteristics of resist films produced by spinning. *J Appl Phys* 1978;49(7):3993–7. <https://doi.org/10.1063/1.325357>.
- Heriot SY, Jones RAL. An interfacial instability in a transient wetting layer leads to lateral phase separation in thin spin-cast polymer-blend films. *Nat Mater* 2005;4 (10):782–6. <https://doi.org/10.1038/nmat1476>.
- Jukes PC, Heriot SY, Sharp JS, Jones RAL. Time-resolved light scattering studies of phase separation in thin film semiconducting polymer blends during spin-coating. *Macromolecules* 2005;38(6):2030–2. <https://doi.org/10.1021/ma0477145>.
- Chauhan M, et al. Investigating two-step MAPbI₃ thin film formation during spin coating by simultaneous: *in situ* absorption and photoluminescence spectroscopy. *J Mater Chem A Mater* 2020;8(10):5086–94. <https://doi.org/10.1039/c9ta12409h>.
- Alhazmi N, Pineda E, Rawle J, Howse JR, Dunbar ADF. Perovskite crystallization dynamics during spin-casting: an *in situ* wide-angle X-ray scattering study. *ACS Appl Energy Mater* 2020;3(7):6155–64. <https://doi.org/10.1021/acsaem.9b02470>.
- Barri D, Tang MC, Munir R, Li R, Zhao K, Smilgies DM. Processing of lead halide perovskite thin films studied with *in-situ* real-time X-ray scattering. *ACS Appl Mater Interfaces* 2022;14(23):26315–26. <https://doi.org/10.1021/acami.2c03153>.
- Ebbens S, et al. *In situ* imaging and height reconstruction of phase separation processes in polymer blends during spin coating. *ACS Nano* 2011;5(6):5124–31. <https://doi.org/10.1021/nn201210e>.
- Toolan DTW, Hodgkinson R, Howse JR. Stroboscopic microscopy - Direct imaging of structure development and phase separation during spin-coating. *J Polym Sci B Polym Phys* 2014;52(1):17–25. <https://doi.org/10.1002/polb.23288>.
- Toolan DTW, et al. Direct observation of morphological development during the spin-coating of polystyrene-poly(methyl methacrylate) polymer blends. *J Polym Sci B Polym Phys* 2013;51(11):875–81. <https://doi.org/10.1016/j.solmat.2013.02.030>.
- Bergqvist J, Mauger SA, Tvingstedt K, Arwin H, Inganäs O. *In situ* reflectance imaging of organic thin film formation from solution deposition. *Sol Energy Mater Sol Cells* 2022;14(23):26315–26. <https://doi.org/10.1016/j.solmat.2013.02.030>.
- Birnie DP, Haas DE, Hernandez CM. Laser interferometric calibration for real-time video color interpretation of thin fluid layers during spin coating. *Opt Lasers Eng* 2010;48(5):533–7. <https://doi.org/10.1016/j.optlaseng.2009.12.021>.
- Heavens OS. Optical properties of thin films. *Rep Prog Phys* 1960;23(1). <https://doi.org/10.1080/0713818200>.
- Frostad JM, Tammaro D, Santollani L, Bochner de Araujo S, Fuller GG. Dynamic fluid-film interferometry as a predictor of bulk foam properties. *Soft Matter* 2016; 12(46):9266–79. <https://doi.org/10.1039/C6SM01361A>.
- Sett S, Sinha-Ray S, Yarin AL. Gravitational drainage of foam films. *Langmuir* 2013;29(16):4934–47. <https://doi.org/10.1021/la4003127>.
- Gustafsson L, Högglund E, Marklund O. Measuring lubricant film thickness with image analysis. *Proc Inst Mech Eng Part J J Eng Tribol* 1994;208(3):199–205. https://doi.org/10.1243/PIME_PROC_1994_208_371_02.
- Goto E, Dogru M, Kojima T, Tsubota K. Computer-synthesis of an interference color chart of human tear lipid layer, by a colorimetric approach. *Invest Ophthalmol Vis Sci* 2003;44(11):4693–7. <https://doi.org/10.1167/iovs.03-0260>.
- Zhang Y, Sharma V. Domain expansion dynamics in stratifying foam films: experiments. *Soft Matter* 2015;11(22):4408–17. <https://doi.org/10.1039/c5sm00066a>.
- Chandran Suja V, Sentmanat J, Hofmann G, Scales C, Fuller GG. Hyperspectral imaging for dynamic thin film interferometry. *Sci Rep* 2020;10(1):1–8. <https://doi.org/10.1038/s41598-020-68433-0>.
- Willert C, Stastick B, Klinner J, Moessner S. Pulsed operation of high-power light emitting diodes for imaging flow velocimetry. *Meas Sci Technol* 2010;21(7). <https://doi.org/10.1088/0957-0233/21/7/075402>.
- Sherman R. Carbon dioxide snow cleaning. *Part Sci Technol* 2007;25(1):37–57. <https://doi.org/10.1080/02726350601146424>.
- Birnie DP. Combined flow and evaporation during spin coating of complex solutions. *J Non Cryst Solids* 1997;218:174–8. [https://doi.org/10.1016/S0022-3093\(97\)00141-5](https://doi.org/10.1016/S0022-3093(97)00141-5).
- Birnie DP, Manley M. Combined flow and evaporation of fluid on a spinning disk. *Phys Fluids* 1997;9(4):870–5. <https://doi.org/10.1063/1.869519>.

- [38] Heikkinen V, Lenz R, Jetsu T, Parkkinen J, Hauta-Kasari M, Jääskeläinen T. Evaluation and unification of some methods for estimating reflectance spectra from RGB images. *J Opt Soc Am A* 2008;25(10):2444. <https://doi.org/10.1364/josaa.25.002444>.
- [39] Luňáček J, Hlubina P, Luňáčková M. Simple method for determination of the thickness of a nonabsorbing thin film using spectral reflectance measurement. *Appl Opt* 2009;48(5):985–9. <https://doi.org/10.1364/AO.48.000985>.
- [40] Kim K, Kwon S, Pahk HJ. Fast analysis of film thickness in spectroscopic reflectometry using direct phase extraction. *Curr Opt Photonics* 2017;1(1):29–33. <https://doi.org/10.3807/COPP.2017.1.1.029>.

Jack Atkinson - Attained his integrated master's degree in chemical engineering from the University of Sheffield's Chemical and Biological Engineering Department 2021. His dissertation was based on Industry 4.0 software development and data visualization. He is

currently undergoing his PhD studies in the same department, supervised by Professor Jonathan Howse. His focus is on using reflection and scattering of thin films to direct fabrication processes in both spin-coating and slot-die coating and he is due to submit his PhD thesis in early 2025.

Professor Jonathan Howse - Obtained a PhD from the University of Sheffield in 1999. He then spent two years at TU-Berlin whilst also working as a beamline scientist at the Hahn-Meitner-Institute, before returning to Sheffield to as a postdoctoral research assistant working with Professor Tony Ryan and Professor Richard Jones. He joined the Department of Chemical & Biological Engineering as a Lecturer in 2007 and has pioneered research on *in-situ* studies of spin coating soft matter, polymer vesicle formation and colloidal nano-swimmers. He was made a professor of polymer engineering in 2021 and is currently focusing research on responsive manufacturing in roll-to-roll coating systems.